

1 **The effect of fault architecture on slip behavior in shale**
2 **revealed by distributed fiber optic strain sensing**

3 **Chet Hopp¹, Yves Guglielmi¹, Antonio Pio Rinaldi^{2,1}, Florian Soom¹, Quinn**
4 **Wenning⁴, Paul Cook¹, Michelle Robertson¹, Maria Kakurina⁵, and Alba**
5 **Zappone^{2,3}**

6 ¹Lawrence Berkeley National Laboratory; Earth and Environmental Sciences Area, Berkeley, CA, USA

7 ²Swiss Seismological Service, ETH Zürich, Zürich, Switzerland

8 ³Department of Mechanical Engineering, ETH Zürich, Zürich, Switzerland

9 ⁴Department of Earth Sciences, ETH Zürich, Zürich, Switzerland

10 ⁵University of Neuchâtel, CHYN, Emile-Argand 11, 2000, Neuchâtel, Switzerland

11 **Key Points:**

- 12 • Slow slip on a fault zone in a clay caprock concentrates on two interfaces with the
13 intact host rock, because the fault displays no damage zone.
- 14 • Distributed strain sensing (DSS) shows equal measurand performance to standard
15 borehole potentiometers, with better spatial resolution and sensitivity to shear.
- 16 • Activated and unactivated fractures share similar orientations; activated fractures
17 are weaker due to the presence of scaly clay.

Corresponding author: Chet Hopp, chopp@lbl.gov

Abstract

We use Distributed Strain Sensing (DSS) through Brillouin scattering measurements to characterize the reactivation of a fault zone in shale (Opalinus clay), caused by the excavation of a gallery at ~ 400 m depth in the Mont Terri Underground Laboratory (Switzerland). DSS fibers are cemented behind casing in six boreholes cross-cutting the fault zone. We compare the DSS data with co-located measurements of displacement from a chain potentiometer and a three-dimensional displacement sensor (SIMFIP). DSS proves to be able to detect in- and off-fault strain variations induced by the gallery excavated 30–50 m away. The total permanent displacement of the fault is ~ 200 microns at rates up to 1.5 nm/sec. DSS is sensitive to longitudinal and shear strain with measurements showing that fault shear is concentrated at the top and bottom interfaces of the fault zone with little deformation within the fault zone itself. Such a localized pattern of strain relates to the architecture of the fault that is characterized by a thick, weak layer, slipping at the edges, with no surrounding damage zone. Overall, DSS shows that slow slip may activate everywhere there is a weak fault within a shale series. Thus, our work demonstrates the importance of shear strain on faults caused by remote loading, highlighting the utility of DSS systems to detect and quantify these effects at large reservoir scales.

1 Plain language summary

Understanding how and why faults move in anisotropic shales is important for assessing the integrity of caprocks overlying geologic CO₂ sequestration sites or increasing efficiency of hydraulic fracturing operations in shale gas reservoirs. Here we show that fiber optic cables can be used to accurately measure fault slip when cemented inside boreholes that intersect such a structure. This allows detecting and monitoring of a larger volume of rock than ever before. Our measurements show that a kilometers-long fault in a clay rock, when disturbed by the excavation of a tunnel ~ 30 m away, displayed localized slip mostly along its upper and lower interfaces, in contrast to a more distributed slip as would be expected with a more “classical” fault core-damage zone architecture. In addition, the excavation produced slip on other, smaller fractures, with slip on these planes sometimes exceeding the slip on the larger fault. These observations show how important slow slip in anisotropic shales can be in accommodating remote loading (e.g. deep reservoir pressurization or hydraulic fracturing). DSS offers new insight into whether

49 slow slipping faults can trigger significant caprock leakage and induce earthquakes dur-
50 ing deep injection operations.

51 **2 Introduction**

52 Understanding the mechanics of fault and fracture movement in anisotropic shales
53 is important for estimating the integrity of caprocks overlying geologic CO₂ sequestra-
54 tion sites or for improving the efficiency of hydraulic fracturing stimulations of shale gas
55 reservoirs. Indeed, by combining reservoir-scale, geophysical data with laboratory results,
56 Zoback et al. (2012) suggest that hydrofracturing might cause significant slow slip on sur-
57 rounding fractures and faults in shale rocks, particularly when clay content exceeding
58 30% favors stable sliding instead of unstable slip (i.e. microseismicity). Looking at the
59 decameter scale around underground galleries in the Opalinus clay shales in Mont Terri
60 Rock Laboratory (Switzerland), Amann et al. (2018) highlight that a high density of bed-
61 ding planes and faults strongly influences macroscopic failure through shearing along pre-
62 existing planes coupled to newly created extensional fractures. Compiling laboratory de-
63 termined mechanical properties of various types of shales, Bourg (2015) shows a factor
64 of 20 decrease of the unconfined compressive strength of shales that contain $\sim 1/3$ phyl-
65 losilicate (clay mineral) mass fraction. It is therefore important to better characterize
66 how rupture can develop macroscopically in a thick shale layer since it may substantially
67 change stress and favor leakage flowpath creation. For example, field experiments (Guglielmi
68 et al., 2020) and laboratory tests (Gutierrez et al., 2000) show that even small amounts
69 of shear can lead to significant modifications of the hydraulic properties of fractured and
70 mechanically anisotropic shales.

71 Given this context, optical fiber-based sensors may offer the possibility to track how
72 widely-distributed shear may be in thick anisotropic shale series. A broad array of sci-
73 entific and engineering applications have sprung up in the past few decades around the
74 use of fiber optics as distributed measurement devices (so-called distributed fiber optic
75 sensing, DFOS). These techniques leverage light that is scattered in the opposite direc-
76 tion of a passing optical pulse and, by measuring the frequency and gain of these backscat-
77 tered components, can be used for sensing purposes. The result is a quasi-continuous sen-
78 sor capable of being deployed in harsh environments and over distances of several kilo-
79 meters (Hartog, 2017).

80 In this study we focus on measurements of the longitudinal strain of the sensing
81 fiber through interrogation of the Brillouin component of backscattered light. Distributed
82 Brillouin sensing (referred to here as distributed strain sensing, DSS) has found myriad
83 applications since its inception in the 1990's, mostly monitoring the state-of-health of
84 various elements of critical infrastructure including the telecommunications fibers them-
85 selves (Tateda et al., 1990), the underground tunnels that house them (Naruse et al., 2005),
86 nuclear waste repositories (Delepine-Lesoille et al., 2012), roads (Iten et al., 2008), lev-
87 ees (Naruse, 1999), and the stability of critical slopes (jun Wang et al., 2008).

88 Distributed fiber optics have also been deployed in deep boreholes, initially for mon-
89 itoring of borehole casing integrity in oil and gas reservoirs (Zhou et al., 2010) but, more
90 recently, downhole DSS has been used to monitor pumping-induced compaction (C.-C. Zhang
91 et al., 2018), track the progression of hydraulic fractures in unconventional oil and gas
92 reservoirs (Z. Zhang et al., 2020), and measure injection-induced strains in shallow aquifers
93 (Sun et al., 2020). While these studies convincingly demonstrated the ability of DSS to
94 measure strains on the order of tens of microstrains ($\mu\epsilon$), borehole-based measurements
95 are inherently difficult to verify due to inaccessibility and the difficulty of deploying sep-
96 arate instruments within a single borehole.

97 Two previous studies have made an attempt to ground truth DSS strain measure-
98 ments in grouted boreholes. Krietsch et al. (2018) monitored a series of hydraulic stim-
99 ulation tests in the Grimsel underground lab with co-located DSS and Fiber Bragg Grat-
100 ings (FBGs). Using the FBG system as the 'true' measure, the authors determined that
101 the DSS system provided good qualitative agreement with the FBG system but poor tem-
102 poral and measurand resolution. They also observed poor agreement in the magnitude
103 of the measured strains. Valley et al. (2012) grouted fibers into a sill pillar that was ac-
104 tively undergoing mining and attempted to corroborate the measurements using co-located
105 extensometers. They also concluded that, while the DSS measurements were qualitatively
106 in agreement with the extensometer, the measurements were not useful in quantifying
107 the strain in the borehole. Both of these studies highlight the ongoing need for field test-
108 ing and independent corroboration of DSS measurements in grouted boreholes.

109 Here we present measurements from a suite of seven boreholes intersecting a fault,
110 hereafter referred to as the Main Fault, in the Mont Terri Rock Laboratory (MTRL, Switzer-
111 land). These boreholes are part of an experimental setup aimed at studying the effect

112 of CO₂ injection and pressurization (CS-D and FS-B projects; Zappone et al., 2020; Guglielmi
113 et al., 2018) on the deformation and permeability of a fault zone affecting the Opalinus
114 clay, a low permeability rock considered an analog to a reservoir caprock (Bossart et al.,
115 2017). Six of the seven boreholes are instrumented with a loop of single-mode fiber op-
116 tic cable, grouted behind casing or anchored to inflatable packer assemblies. The bore-
117 holes also contain displacement sensors, including a chain potentiometer and a three-dimensional
118 displacement sensor called the SIMFIP (Guglielmi et al., 2013), which are co-located/proximal
119 with the fiber optic loops and allow us to tune our DSS measurements.

120 Our study details the mechanical response of the thick, faulted, and anisotropic Opal-
121 inus clay to stress transferred from the excavation of a new gallery in the MTRL. We first
122 use this opportunity to demonstrate the sensitivity of our multi-borehole fiber array to
123 the movement occurring within the Main Fault zone in response to a remote triggering
124 event. We then use these measurements to characterize the macroscopic activation of the
125 various Opalinus clay structures. Thanks to the independent displacement measurements
126 from co-located or proximal sensors with respect to the fibers, we demonstrate clear con-
127 sistency between the strain magnitude and temporal occurrence captured between sen-
128 sors. We discuss how stress and fault weakness related to its material content and ar-
129 chitecture control the observed distributed slip.

130 **2.1 Fault activation experiments at the Mont Terri Rock Laboratory**

131 The Mont Terri Rock Laboratory, operated by the Swiss Geological Survey, is lo-
132 cated on one limb of a fault-bend anticline within a low-permeability claystone unit known
133 as the Opalinus clay (Bossart et al., 2017; Hostettler et al., 2017). The Opalinus clay is
134 both a potential target formation for Switzerland’s nuclear waste repositories and a use-
135 ful cap rock analog for CO₂ sequestration (Bossart et al., 2017). Additionally, the gal-
136 leries of the MTRL are intersected by a kilometer-scale thrust fault zone, the so-called
137 Main Fault (Jaeggi et al., 2017), which offers researchers the opportunity to investigate
138 the effect of fault activation on the leakage potential of a self-sealing clay unit (Guglielmi
139 et al., 2017, 2020; Birkholzer, 2018; Zappone et al., 2020). The Mont Terri Main Fault
140 consists of a thrust zone, 1 to 3 m in width, bounded by two major fault planes char-
141 acterized by a strike of N066° to N075° and a dip of 45° to 65°SE (Figure 1).

142 The CS-D and FS-B projects, directed by ETH Zürich and Lawrence Berkeley Na-
 143 tional Lab (LBNL), respectively, are focused on understanding how a minor fault affect-
 144 ing a clay unit (i.e. caprock) might respond to the long term injection of CO₂ (Zappone
 145 et al., 2020). The two projects are highly complementary. The CSD project is looking
 146 at small ~ 0.05 ml/min injection of a CO₂ brine into the fault below the fault activation
 147 pressure. It is mainly focusing on long term hydro-mechanical and chemical processes
 148 of fluid diffusion at meter-scale in the fault zone (Zappone et al., 2020). The FS-B project
 149 is looking at large-scale (>5 L/min) injection into the fault above activation pressure.
 150 It is focused on hydromechanical processes at 10-meter scale during fault rupture, in-
 151 cluding the potential for induced seismicity, and during inter-rupture periods (Guglielmi
 152 et al., 2018).

153 A 70-m x 70-m x 70-m volume, crosscut by the Main Fault, is instrumented with
 154 23 boreholes hosting various systems recording pressure and flow rate into multiple in-
 155 jection intervals, active and passive-source seismicity, electrical resistivity, fluid and gas
 156 geochemistry, and geomechanical strain/displacement/tilt. Figure 1 shows all boreholes
 157 drilled by CS-D/FS-B. Here we focus on the CS-D boreholes (colored in the foreground
 158 of Figure 1). The FS-B boreholes are shown in gray in the background.

159 **3 Monitoring network and remote gallery excavation**

160 The depth of the Main Fault zone intersection with each borehole, as verified by
 161 image logging and core, varies from 11 to 28 m below the gallery floor (Table 1). The
 162 thickness of the fault zone varies between 1 and 3 meters within the MTRL and is char-
 163 acterized by a laterally heterogeneous mix of fault gouge, C'-type shear bands, scaly clay,
 164 and meso- and micro-scale folds (Nussbaum et al., 2011). Here ‘scaly clay’ refers to a
 165 mass of unaltered, Opalinus microlithons, separated by slickensides, and is pervasive through-
 166 out the Main Fault (Jaeggi et al., 2017). Fault planes within the Main Fault zone are
 167 mostly oriented subparallel to the fault zone itself, but also include a set of fractures nor-
 168 mal to it (Zappone et al., 2020; Wenning et al., 2020). In addition, a series of ENE-striking,
 169 bedding-parallel fractures, with similar strike but shallower dip than the Main Fault, are
 170 intersected by the CS-D boreholes (Zappone et al., 2020). Bedding in the Opalinus is
 171 oriented subparallel to the Main Fault, striking N055°, and dipping SE046°, roughly 15°
 172 shallower than the Main Fault.

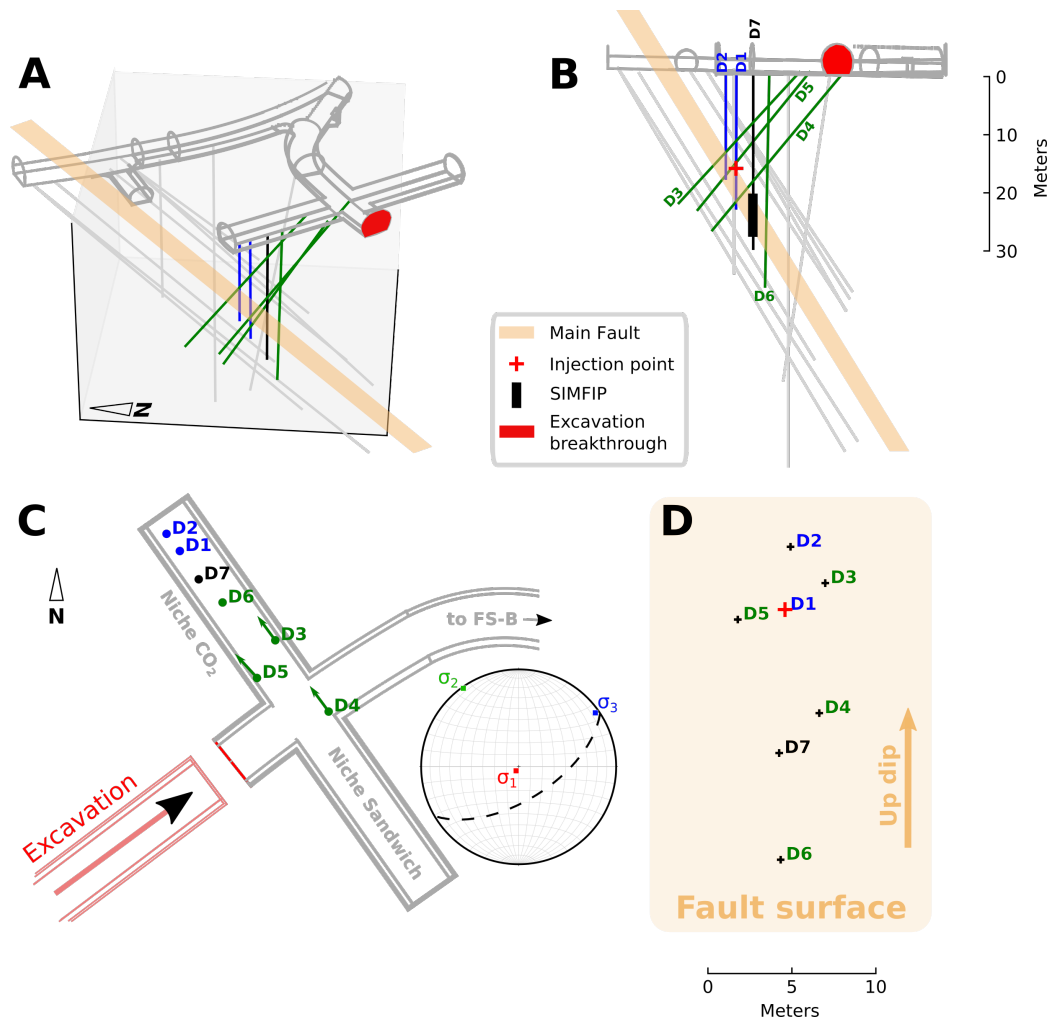


Figure 1. A) 3D perspective of the FS-B/CS-D project showing all boreholes colored by use. Blue boreholes D1 & D2 are injection and pressure monitoring boreholes, green boreholes contain monitoring systems, and the black borehole, D7, contains the SIMFIP displacement sensor. Light gray boreholes in the background are FS-B boreholes. All boreholes are instrumented with distributed fiber optic sensors except D7 B) Cross-section along Niche CO₂ with the injection point in D1 indicated by a red cross. C) Map view of the borehole collar locations in Niche CO₂ and lower hemisphere stereonet projection of the principal stress axes estimated by Guglielmi et al. (2020). Dotted line shows the approximate orientation of the Main Fault D) Intersection points for each well with the top of the Main Fault

Borehole name	Main Fault top [m]	Main Fault bottom [m]
BCS-D1	14.34	19.63
BCS-D2	11.04	16.39
BCS-D3	17.98	20.58
BCS-D4	27.05	28.44
BCS-D5	19.74	22.66
BCS-D6	28.5	31.4
BCS-D7	22.46	25.54

Table 1. Depths of the top and bottom of the Main Fault zone in each of the CS-D boreholes

173 Boreholes BCS-D1 through D6 contain a single 3.2 mm-diameter loop of BRUSensTM
174 strain sensing cable that itself comprises a single optical fiber hermetically sealed and
175 strain-locked within a metal tube and an outer nylon sheath. These cables are designed
176 to measure strains of up to 1% (10000 $\mu\epsilon$). In BCS-D1 and D2 (blue boreholes, Figure
177 1), the fiber optic cable (BRUSens 3.2 mm V4 metallic) is anchored by a compression
178 ferrule at the top of each injection interval (with four and six intervals in D1 and D2,
179 respectively). However, the fiber optic cables in these boreholes were not monitored at
180 the time of the excavation detailed here and so are omitted from the data analysis.

181 In boreholes BCS-D3, D4, D5, and D6, the fiber (BRUSens 3.2 mm V9 grip) is ce-
182 mented behind the PVC casing using a grout mix of 81.9 L water, 4.9 kg bentonite, and
183 50.1 kg cement (green boreholes, Figure 1). This provides a truly continuous measure-
184 ment along the entire length of each borehole. In these cases, the nylon cable jacket is
185 textured to provide optimized strain coupling between the fiber and the grout so that,
186 in theory, only the grout strain is being measured, with the assumption made that the
187 grout is coupled to the host rock. Each of these boreholes also includes a single resin ‘plug’
188 to mitigate against fluid traveling along the cemented annulus (Figure 2B). These plugs
189 are 0.5–2 m thick sections where the resin replaces the grout in the annulus between the
190 borehole wall and the PVC casing. Borehole diameter ranges from 101 to 146 mm, with
191 consistent PVC casing diameters of 80 mm.

192 The fiber loops in each borehole are connected into a multi-borehole circuit and
193 interrogated by an Omnisens DITEST VISION Dual temperature and strain unit using
194 the Brillouin Optical Time Domain Analysis technique (Horiguchi & Tateda, 1989).

195 In borehole BCS-D5, a chain of 12 potentiometers is cemented behind casing along-
196 side the fiber-optic loop in borehole BCS-D5 (Zappone et al., 2020; Rinaldi et al., 2020).
197 Each potentiometer is connected to the adjacent units by a PVC tube and measures bore-
198 hole axial displacement relative to the neighboring units with a maximum displacement
199 of 100 mm. This chain of potentiometers provides a co-located measurement of displace-
200 ment with respect to the optical fibers, allowing us to directly verify the measurements
201 made with the DSS system.

202 In borehole BCS-D7, a combined three-dimensional-displacement, pressure, and fluid
203 electrical conductivity probe, the SIMFIP (Guglielmi et al., 2013), is clamped above and
204 below the Main Fault. The clamps are 6.3 meters apart allowing the SIMFIP to mea-
205 sure the relative displacement across the entire Main Fault zone. The instrument uses
206 six fiber-bragg gratings attached to a bespoke aluminum cage to resolve the full 3D dis-
207 placement field with micrometer precision. The SIMFIP is alone in BCS-D7, and there-
208 fore is not co-located with any portion of the fiber optic loop. Understanding this lim-
209 itation, here we use its three-dimensional fault displacement measurement in compar-
210 ison to the DSS data.

211 4 Excavation of Gallery 18

212 Excavation of Gallery 18 began on 14 March 2018, and lasted for more than one
213 year. During much of this time, the excavation front was far from Niche CO₂, which, it-
214 self, was completed in May 2018. The installation of the CS-D systems occurred between
215 August and December 2018. During the first half of 2019, the final stages of excavation
216 proceeded towards Niche CO₂ as indicated in Figure 1. Excavation passed along the strike
217 of the Main Fault at a constant ~ 23 m distance from the upper fault zone interface. Break-
218 through occurred adjacent to the CS-D experiment on 27 May 2019 (red faces in Fig-
219 ure 1). Prior to the breakthrough, movement was not detected by the SIMFIP and po-
220 tentiometers at CS-D until 22 May 2019, when the excavation front was ~ 26 m from the
221 SIMFIP. Coincidentally, 22 May was also the date that the DSS system began record-
222 ing. We therefore focus on the period between 22 May and 3 June 2019.

223 5 Methods and processing

224 5.1 Distributed strain sensing

225 When a laser pulse is sent along an optical fiber, some amount of that light is scat-
 226 tered backwards by its interaction with changes in the refractive index of the fiber. There
 227 are three components of this backscattered light relevant to DFOS: one is elastic (Rayleigh)
 228 and two are inelastic (Raman and Brillouin). We are concerned here with the Brillouin
 229 component, which arises from an incident photon’s interaction with crystal lattice vi-
 230 brations that hold some of the optical fiber’s heat. As the interaction is inelastic, the backscat-
 231 tered light is frequency shifted by some amount that linearly depends on the tempera-
 232 ture and strain in the fiber. This relationship is described by Horiguchi and Tateda (1989)
 233 as:

$$\Delta\nu_B = \frac{\partial\nu_B}{\partial\epsilon}\Delta\epsilon + \frac{\partial\nu_B}{\partial T}\Delta T \quad (1)$$

234 where $\Delta\nu_B$ is the change in Brillouin frequency shift for given changes in strain,
 235 $\Delta\epsilon$, and temperature, ΔT . $\frac{\partial\nu_B}{\partial\epsilon}$ and $\frac{\partial\nu_B}{\partial T}$ are the strain and temperature change coeffi-
 236 cients, respectively, which for this work are 500 MHz/% and 1.0 MHz/°C.

237 Using Equation 1, the DITEST interrogator determines the combined temperature
 238 and strain contribution to the measured Brillouin frequency shift. Each measure is then
 239 related to a given point along the fiber by recording the launch and arrival time of the
 240 probe pulse with respect to the speed of light. Because the light pulse from the inter-
 241 rogator has a finite length, measurements are averaged over the corresponding length of
 242 fiber. This is referred to as the spatial resolution (or often the ‘gauge length’). The Brill-
 243 ouin frequency shift for one gauge length is reported as a single measurement at a point
 244 along the fiber that we call a ‘channel’. The spatial sampling and spatial resolution were
 245 0.26 and 0.5-to-1.0 meters, respectively, for each of the periods of our study. Notice that
 246 the channel spacing is less than the spatial resolution. Therefore, the DSS measurement
 247 is a sliding window with a width equal to the spatial resolution, slid along the fiber in
 248 increments defined by the spatial sampling.

249 Because the Brillouin frequency shift is sensitive to both temperature and strain
 250 changes, a number of methods are employed to deconvolve their contributions. Often,
 251 an independent measurement of temperature (for example from a Raman scattering sys-

tem) is used to remove the temperature contribution from the Brillouin measurements. Alternatively, a “strain free” cable is somehow decoupled from the system of interest and can be co-located with a coupled cable and connected in series. In our case we had access to neither, but we make the assumption that the temperature change within our testbed is negligible with respect to the changes in Brillouin shifts being measured (Madjdabadi et al., 2014, 2016; Hartog, 2017).

5.2 Borehole mapping and measurement symmetry

As mentioned above, for any given distributed strain measurement, its distance along the fiber is accurately known from the two way travel time in relation to the speed of light. Translating this distance into a borehole coordinate requires a process of ‘mapping’ whereby the distances along-fiber are matched to the known locations of the features we want to measure (in this case boreholes BCS-D1–D6). We decide to map distance to location by observing a single Brillouin frequency shift measurement along the entire fiber length (i.e. one time sample; Figure 2A). Because the fiber is installed as a loop in each borehole, we expect there to be symmetry in the measurements about the bottom of the boreholes. In other words, the downgoing and upgoing legs of the fiber in a given borehole should measure roughly the same strain.

For the case of our experiment, the BRUsens cable is grouted into the boreholes (or attached to the casing above the packers in D1 and D2) while the sections of fiber between boreholes are standard patch cables lying in a cable tray along the gallery wall. The difference in fiber coating and installation produce an obvious difference in the Brillouin frequency measurement that allows us to map the along-fiber distances corresponding to the entry and exit points for each borehole. In Figure 2A, the entry and exit points for each borehole are indicated by dotted lines, with the bottom shown as a single solid line. The mapped along-fiber lengths agree with field measurements of the cable lengths set in the gallery. By manually selecting the point of greatest symmetry for each borehole and accounting for their known drilled depths, we isolate the slice corresponding to each borehole.

The process of borehole mapping should, in theory, result in two parallel sections (legs) of fiber in each borehole; one downgoing and one upgoing. Assuming that each is measuring approximately the same strain field, the measurements should be equal be-

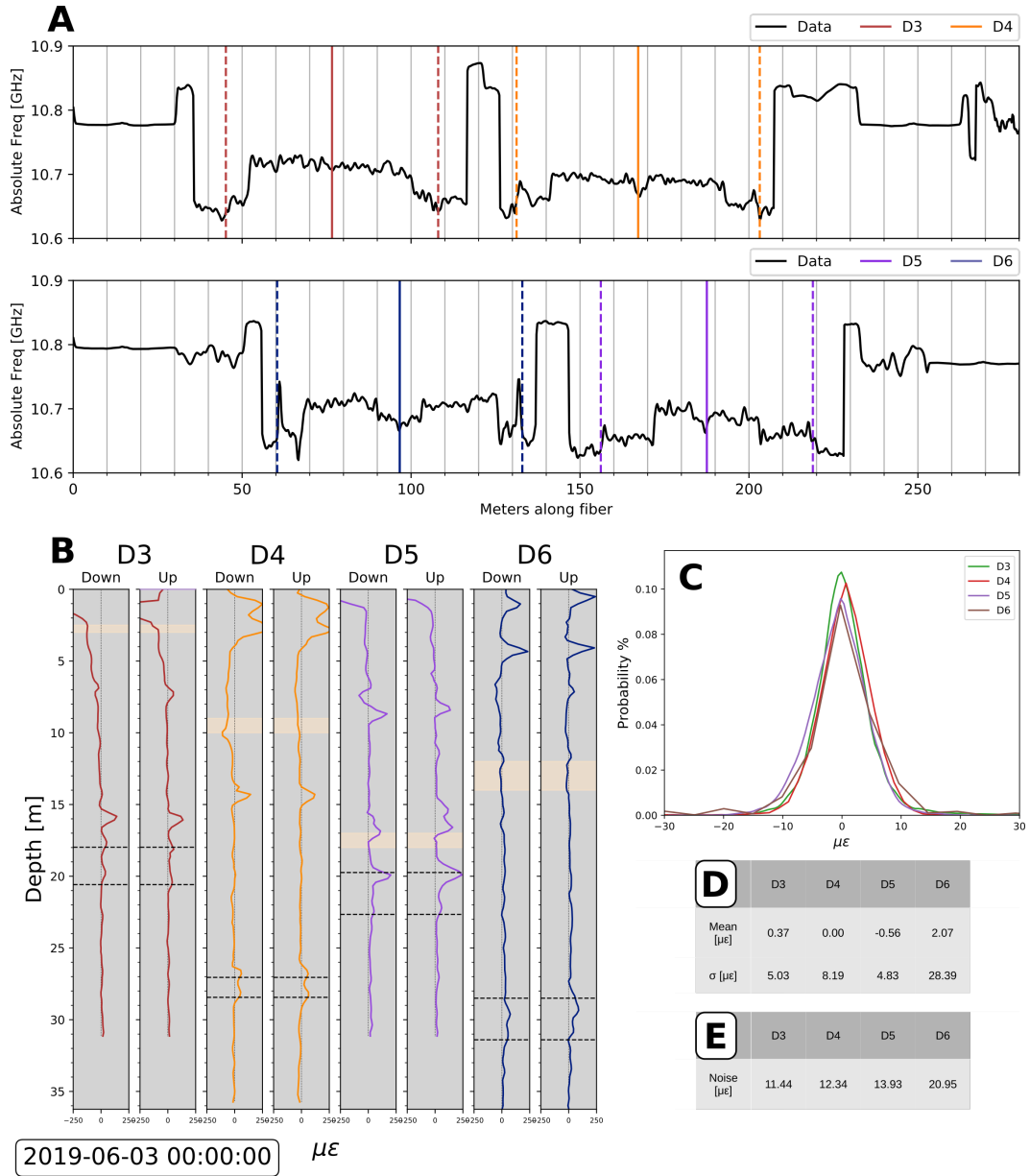


Figure 2. A) Absolute frequency along the length of the fiber during gallery excavation. The two panels correspond to two separate fiber optic loops, each with two boreholes. Boreholes D1 and D2 were not monitoring during the excavation. B) Distributed strains on the down and up-going leg of each on 3 June 2019, following the breakthrough of the excavation front on 27 May 2019. The depth to the Main Fault is marked with dotted lines, resin plugs are shown in beige. C) Kernel density estimates for the difference between the up-going and down-going legs of fiber in each borehole D) Statistics describing the difference between down and up-going fibers for each borehole E) Average 3-standard-deviation noise for each borehole.

283 tween up and down-going fiber for a given depth. Figure 2B shows both the down and
 284 up-going fiber leg in each borehole on 3 June 2019, following the breakthrough of the ex-
 285 cavation on 27 May. The symmetry in the measurements between fiber legs is visually
 286 apparent. The depths at which the measurements are not symmetric typically coincide
 287 with depths where the fiber is expected to be poorly coupled to the rock mass, for ex-
 288 ample at the borehole collar or at the depths where grout is replaced by the resin plugs
 289 (beige bands, Figure 2B). But while the symmetry of the measurements between down
 290 and upgoing legs is evident, the absolute value measured at a given depth on either leg
 291 can vary significantly. This is likely a result of heterogeneous coupling of the fiber to grout
 292 and the grout to the rock mass. This could be the result of changes in the distribution
 293 of grout (e.g. air pockets) or to the effect of other equipment installed in the borehole.
 294 For example, in BCS-D5 the chain potentiometer might affect the strain measured on
 295 the fiber closest to it, but have less effect on the opposing leg. Also, for the inclined, grouted
 296 boreholes, the stress state may vary along the borehole circumference. In this case, fiber
 297 legs on opposing sides of the borehole could measure different responses to stress per-
 298 turbation, even for the same depth in the borehole.

299 Figure 2C shows the difference between down and upgoing fiber measurements for
 300 all measurement times and channels, colored by borehole. The statistics for the distri-
 301 butions shown in Figure 2C are reported in Figure 2D. The fact that the distributions
 302 are nearly zero-mean signifies that there is no systematic preference for higher or lower
 303 values measured by one leg with respect to the other. The standard deviations of the
 304 curves in Figure 2D, however, range from 4.83 to 28.39 $\mu\epsilon$. This means that the mea-
 305 sured strain at a given depth in a borehole might vary by tens of microstrains depend-
 306 ing on which leg is selected, significantly increasing the uncertainty in the measured strain.

307 **5.3 Measurement noise**

308 We quantify the measurement noise following Madjdabadi et al. (2016). For each
 309 channel in a borehole, we calculate 3 standard deviations for a reference time period (with
 310 no expected strain signal). We then average this value over all channels in the sensor,
 311 resulting in a single noise value per borehole (Figure 2E). The noise levels range from
 312 11.44 to 20.95 $\mu\epsilon$, meaning that each segment of the fiber cannot confidently resolve strains
 313 of less than these values.

314 **5.4 Measurement artifacts**

315 Two final artifacts are then removed from the data. The first artifact is an ambi-
 316 guity in the exact position of each channel. The ambiguity arises because the channel
 317 location is reported at the center of the light pulse (for our tests 1.0-m long). But the
 318 strain could be concentrated at any point (or points) inside the pulse. We follow Madjdabadi
 319 et al. (2016) and apply a realignment step detailed in the supplements.

320 The second artifact is a series of systematic shifts in the measured strain for all points
 321 in the fiber. These apparently correlate with shifts in the gain of the signal returned to
 322 the interrogator, although the two values should not be related. We undertook a pro-
 323 cess of removing these shifts for times where the gain also shifted. This process is also
 324 detailed in the supplements.

325 **6 Results**

326 On 22 May 2019, the DSS system was turned on and began to record signals within
 327 the Main Fault zone associated with the excavation of Gallery 18. From 23 May until
 328 the breakthrough on 27 May, there were three episodes of excavation, with the excava-
 329 tion front advancing between 1 and 3 m during each episode. Each episode induced move-
 330 ment on a number of discrete features, including the Main Fault. For each excavation
 331 pulse, the activated features moved at up to 1.5 nm/sec at the onset and decelerated to-
 332 wards a new steady state before accelerating again in response to the next pulse.

333 **6.1 Distribution of deformation revealed by DSS measurements**

334 Fiber-optic strains localized on a number of discrete features within the entire shale
 335 series (Figure 3A). The deformations in the shallow zone (from 0–7 m deep) are up to
 336 one order of magnitude larger than those measured deeper than ~ 7 m (Figure 3B). Bore-
 337 holes D3 and D5 show contractions of >800 and $\sim 600 \mu\epsilon$, respectively. In contrast, D4
 338 and D6 each show two smaller-magnitude peaks of extensional strain, each $\leq 200 \mu\epsilon$. The
 339 differences between the shallow strains in each borehole indicate a complicated strain dis-
 340 tribution in and around the intersection of Gallery 18 and the nearby niches (Figure 1).
 341 In addition, our data show discrete spikes in the strain, highlighting that the deforma-
 342 tion is not broadly distributed but is concentrated on preexisting fractures.

343 The shallow deformations lie within the “limits” of the ‘excavation damage zone’
344 (EDZ; Amann et al., 2018). The EDZ around the CS-D niche (where our boreholes are
345 located) was stable by the time of the Gallery 18 breakthrough detailed in this work (Corkum
346 & Martin, 2007). We are therefore observing the response of the stable, preexisting EDZ
347 as it merges with the new, unstable EDZ surrounding the approaching gallery excava-
348 tion. The strains shown in Figure 3B are the result of these complicated interactions be-
349 tween the new gallery and the preexisting galleries and niches, each with different ori-
350 entations with respect to the far field stress (Figure 1C) and with respect to the dom-
351 inant orientation of the Opalinus bedding (striking NE). This leads to a complicated re-
352 distribution of the local strains, resulting in extension in some locations (D4, D6) and
353 contraction in others (D3, D5). D3 and D5 are drilled with similar orientations from op-
354 posing sides of Niche CO₂ and therefore show a similar shallow strain pattern. D4 and
355 D6 were drilled through portions of the EDZ directly below a gallery and a niche, respec-
356 tively. Given a vertical σ_1 , where the roof and floor of the gallery should converge, it makes
357 sense that D4 and D6 would show extension along the fiber axis. But apart from qual-
358 itative observations, a complicated modeling exercise will be required to shed more light
359 on the patterns shown in Figure 3B.

360 At depths >7 m, strain is localized on several distinct features visible in Figure 3A
361 (indicated by colored arrows). In boreholes D3, D4, and D5, at least one feature is present
362 in a zone that is not the Main Fault, whereas in D6 the Main Fault itself is the only no-
363 table feature. In D3, D4, and D5, off-Main Fault deformations are $>100 \mu\epsilon$, compara-
364 ble to and exceeding the strain measured within the Main Fault zone. Approximately
365 18% of the off-Main Fault fractures identified in core logs correspond to the features in-
366 dicated by arrows in Figure 3A.

367 In all boreholes, strain localizes on the uppermost interface of the fault zone. In
368 D5, ~ 240 microstrain accumulates on this surface, with lesser magnitudes in the other
369 boreholes. Strain also localizes on the lower interface of the fault zone, with relatively
370 little strain measured within the fault zone itself.

371 Compared to the other boreholes, strain in D6 (particularly on the upgoing fiber)
372 appears more distributed over the entire fault zone. D6 is vertical and therefore oblique
373 to the Main Fault. The fiber axis in D6 is therefore more closely aligned with the fault

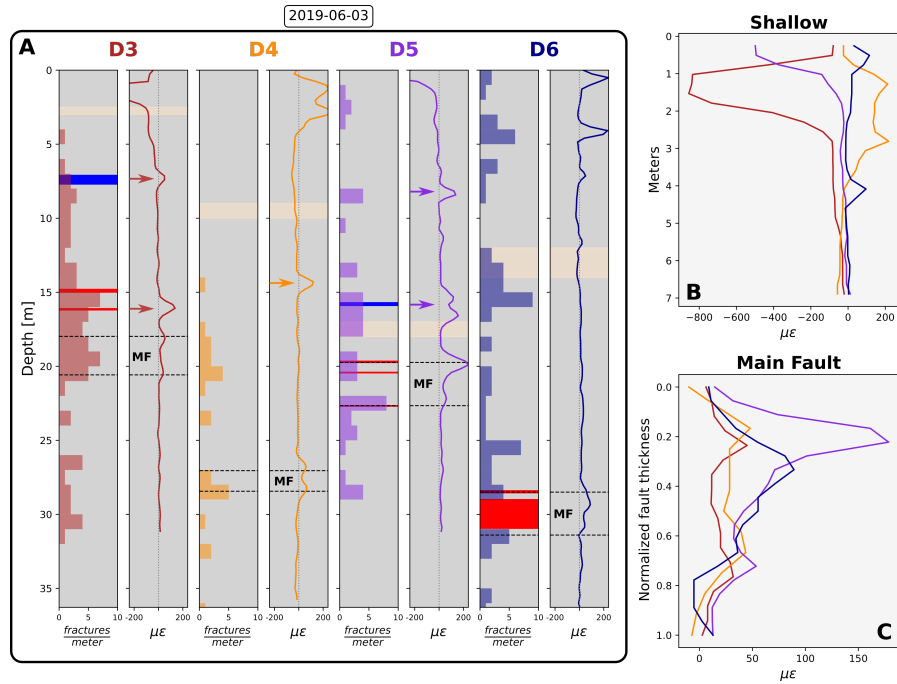


Figure 3. On and off-fault strains - A) Measured strain and fracture density estimated from core. Solid red lines indicated depths of scaly clay identified during core characterization, blue indicates a fracture zone (when not also identified with scaly clay) D4 was drilled with destructive methods so we report fracture density from optical televiewer logs. Resin plugs are in beige, fault top and bottom are indicated by horizontal dotted lines. Arrows show above-fault features recorded on both the up and down-going fibers B) Strains for the upper 7 m of each borehole C) Strains within the fault zone for each borehole. Depths are normalized to the fault zone thickness in each borehole.

374 interface than in D3, D4, or D5, meaning that it may better capture small amounts of
375 shear distributed within the entire fault zone.

376 **6.2 Comparison of DSS measurements to other instruments**

377 In Figure 4A, we show both the chain potentiometer (red) and DSS measurements
378 (purple) in BCS-D5 on 3 June 2019 following excavation breakthrough. The fracture den-
379 sity as estimated from analysis of drill core is shown as a grey histogram. The poten-
380 tiometer string has a variable spatial resolution defined by the spacing of the anchor points
381 between individual elements. We plot these data as a series of steps to account for this.
382 The spacing between elements is smallest across the Main Fault interval (0.5 m). Two
383 other elements of roughly 8 m length are placed above the fault. At the depth of the Main
384 Fault interval, the chain potentiometer and fiber optic measurements both clearly show
385 that most of the movement within the fault interval is concentrated at the uppermost
386 interface, where displacements of 282 μm and 210 μm are measured, respectively. A smaller
387 magnitude peak is also observed at the bottom fault interface, respectively of 80 and 67
388 μm on the potentiometer and DSS. Above the fault, the DSS retains its 1 m spatial res-
389 olution, whereas the potentiometer averages displacements over two 8 meter intervals
390 (from 11–19 m and 2–11 m). Two other large deformations are measured by the DSS;
391 one just above the resin plug (16–17 m) and one at 8 m depth. The chain potentiome-
392 ter, on the other hand, measures no displacement over its shallow intervals due to its lack
393 of spatial resolution.

394 Figure 4B shows a time series comparison between the DSS and the potentiome-
395 ter in BCS-D5. We integrated over the three potentiometer elements at 19.75, 20.25, and
396 20.75 m depths and did the same for the DSS across this depth interval to produce the
397 displacement traces shown. The match between the two instruments is excellent, with
398 a normalized cross correlation coefficient of 0.996 that, when combined with the match
399 shown in Figure 4A, is an indication that the strain magnitudes measured by the DSS
400 system are accurate (if we accept the industry standard potentiometer as a ground-truth).
401 This shows that the DSS can accurately quantify the strain field, thereby complement-
402 ing results from previous studies where DSS could be used only in a qualitative manner
403 (Krietsch et al., 2018; Valley et al., 2012).

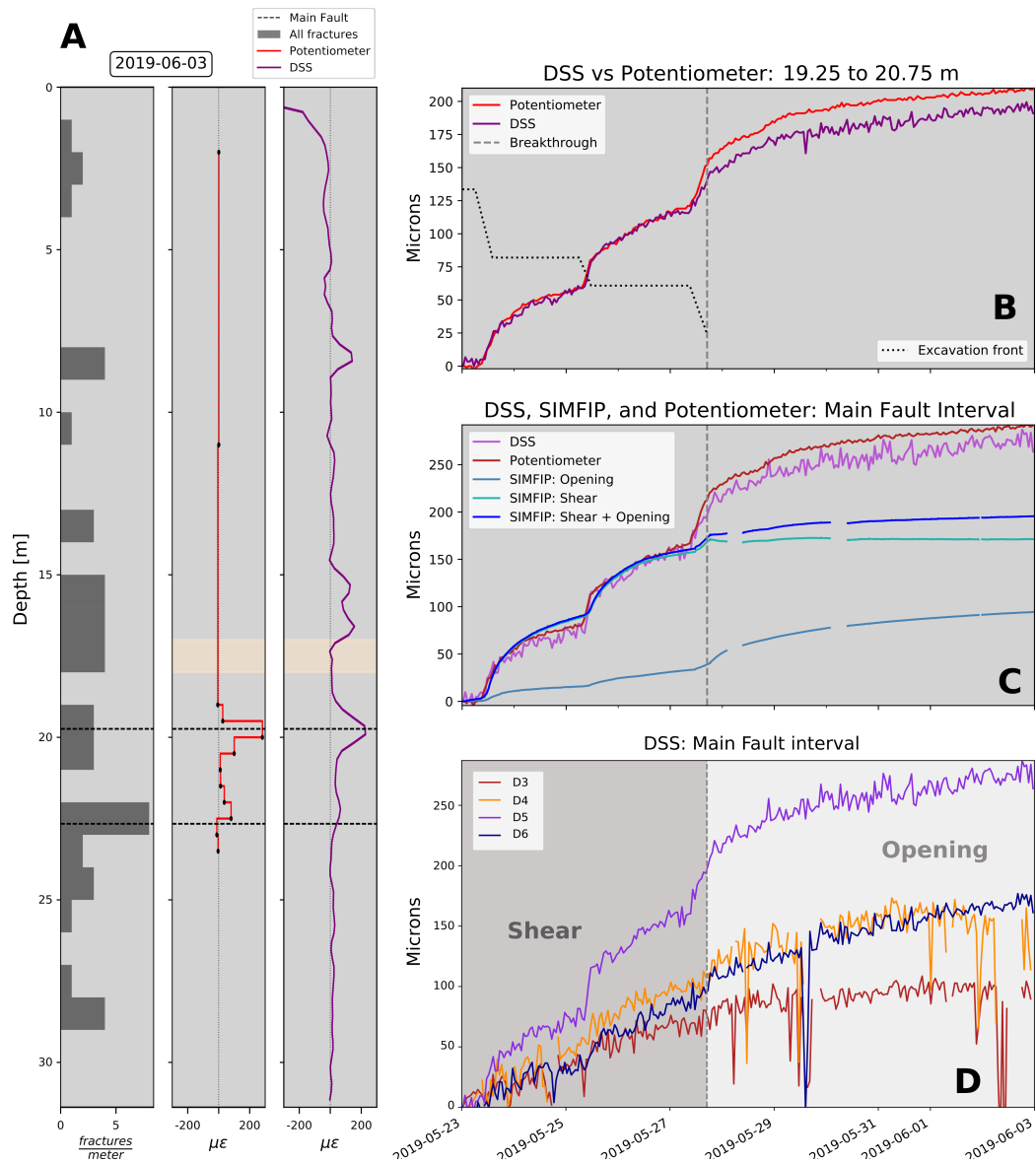


Figure 4. Fault response to gallery excavation - A) Comparison between fracture density, potentiometer extensional strain and DSS strain six days after the breakthrough of Gallery 18 at Niche CO₂. B) Time series comparison between DSS and potentiometer integrated between 19.25 and 20.75 m depth in D5. The dotted line shows the distance of the excavation front to the top of the fault at BCS-D5. The dashed line is the time of the breakthrough C) Potentiometer, DSS, and SIMFIP measurements over the fault zone. SIMFIP total shear is light green and borehole-parallel displacement is gray-blue. The dark blue curve shows the synthetic DSS measurement modeled from SIMFIP data. D) Comparison of DSS displacements integrated across the fault zone in all boreholes.

404 In figure 4D, we compare the temporal evolution of the DSS data integrated across
 405 the Main Fault zone thickness. The Main Fault at D5, being closer to the source of stress
 406 perturbation, shows a larger displacement than the other boreholes. From the perspec-
 407 tive of the DSS fibers, the change in the mode of fault movement is not noticeable. This
 408 is because the fiber measurement is sensitive only to changes along the fiber axis. The
 409 fiber system is obviously sensitive to shear in the Main Fault (see D5, in purple, during
 410 the shear-mode period in the Figure 4D). But the sense of shear, or the transition to open-
 411 mode deformation, is impossible to discern from a single fiber optic sensor.

412 Figure 5 shows the observed deformations in 3-dimensions. Figure 5A shows re-
 413 sults for 25 May 2019, before the breakthrough, while Figure 5B shows observations from
 414 27 May 2019, just after breakthrough. The polygons on the left show the distribution
 415 of displacement on a plane parallel to the fault. For each hour, we performed a linear
 416 interpolation between the integrated DSS measurements in each borehole and the vec-
 417 tor sum of the SIMFIP displacements (all of which are shown in Figure 4C and D). While
 418 the spatial extent of the boreholes is fairly limited, there is a clear negative gradient in
 419 fault zone displacement from left to right (SW to NE) and top to bottom (shallower to
 420 deeper). This is consistent with the orientation of the excavation front, approximately
 421 indicated by the red arrow, which is closest to the Main Fault intersection with D5 and
 422 therefore induces the largest stress perturbation at that point. The black arrow is the
 423 projection of the SIMFIP displacement onto the fault plane for the preceding hour. This
 424 displacement represents an oblique reverse sense of shear across the fault zone, point-
 425 ing in the direction of greatest stress perturbation, in good agreement with the defor-
 426 mation gradient. Following breakthrough, little shear was observed on the Main Fault.

427 We also plot the DSS data in cross section, superimposed on the trajectories of the
 428 boreholes (Figure 5; righthand column). The SIMFIP displacement vector (in the plane
 429 of the cross section) is again shown as a black arrow. The Main Fault interfaces, defined
 430 by their logged depths, are overlain in dotted gray. We also overlay the approximate ori-
 431 entation of the bedding of the Opalinus clay (measured orientation: N055°, dipping SE046°;
 432 green dotted lines, Nussbaum et al., 2011). The depths of the bedding planes shown are
 433 solely schematic, but we have overlain them in such a way that they might correspond
 434 to peaks in strain above the depth of the Main Fault. We suggest that these features cor-
 435 respond to bedding-parallel fractures that were re-activated by the excavation (Amann
 436 et al., 2018). The peaks in the strain curves are not present at all boreholes for some of

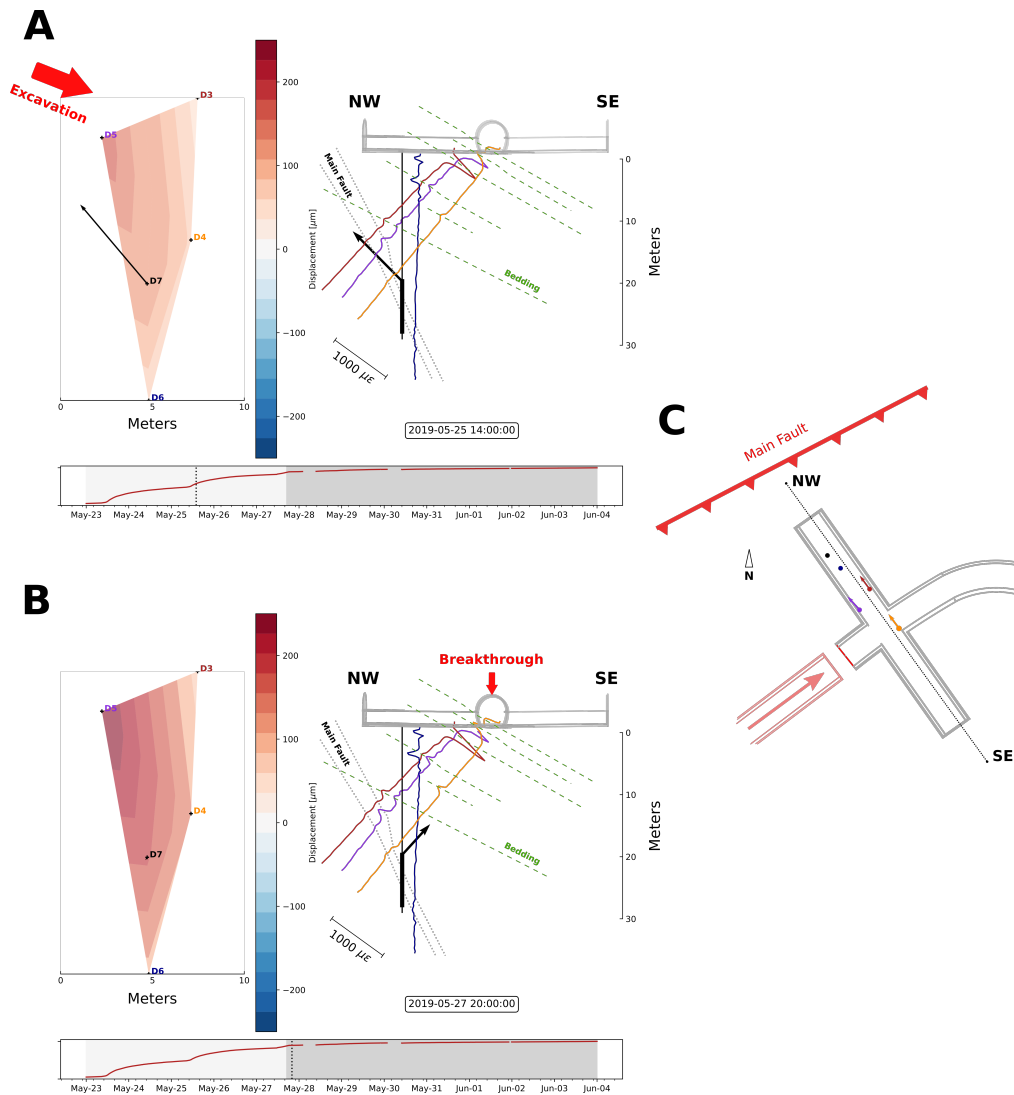


Figure 5. A) Deformation before the excavation breakthrough (26 May) and B) after (1 June; bottom row). The left column shows displacement along the fault plane, linearly interpolated between boreholes. The right column shows a cross-section along Niche CS-D with the strain curves in Figure 3 projected onto the boreholes. Borehole D7 is shown in gray with the SIMFIP indicated by the black box. The direction of SIMFIP displacement (magnitude not to scale) is shown as a black arrow, projected onto the fault plane and the cross-section in the left and right columns, respectively. C) Overview map of Niche CO₂ with the location of the excavated gallery, Main Fault, and boreholes.

437 these proposed fractures, but we note that strain on the Main Fault (for which orien-
 438 tation and depth are well constrained) is equally varied between boreholes. These bed-
 439 ding parallel fractures are pervasive in the Opalinus clay and represent a later stage of
 440 deformation than the Main Fault, possibly even cross cutting it (Nussbaum et al., 2011).

441 7 Discussion

442 7.1 DSS sensitivity to shear and slow slip

443 Although fiber optics are only able to measure changes along the axis of the fibers
 444 themselves (i.e. lengthening or shortening), they can potentially capture shear if the de-
 445 formation field is not perfectly aligned with the fiber’s axis. This is typically the case
 446 when shear is localized on fractures and faults that intersect the monitoring boreholes
 447 at oblique angles. The nature of DSS measurements in shear has been tested in the lab
 448 (e.g. Madjdabadi et al., 2016), but only for a fiber anchored between two points, not grouted
 449 over tens of meters.

450 Here, the SIMFIP instrument installed in BCS-D7 offers a unique opportunity to
 451 estimate the amount of shear applied to the DSS fiber in BCS-D5. We first make the as-
 452 sumption that the displacement measured across the Main Fault at BCS-D7 can be used
 453 as a proxy for displacement at BCS-D5, although the distance between the boreholes is
 454 roughly seven meters along the fault interface and the fault interface dips more steeply
 455 in D5 than in D7. We rotate the SIMFIP displacement tensor into the borehole coor-
 456 dinates of BCS-D5, such that one component is parallel to the borehole axis and the other
 457 two are perpendicular. We then compute the total displacement perpendicular to the
 458 borehole (i.e. total shear). We add the borehole-parallel and borehole-normal compo-
 459 nents of the rotated SIMFIP tensor (vector summation) to give the blue curve that is
 460 shown in Figure 4C. To directly compare this synthetic with the actual DSS and poten-
 461 tiometer measurements, we integrate both across the fault interval. The DSS and po-
 462 tentiometer curves in Figure 4C, still in excellent agreement when integrated across the
 463 fault, closely match the blue SIMFIP curve for the first two excavation pulses. This cor-
 464 responds to the period of shear-mode deformation of the Main Fault. This tells us that
 465 the distributed DSS and potentiometer measurements are sensitive to more than sim-
 466 ply borehole-parallel displacements, instead measuring the correct magnitude of applied
 467 shear as well. Interestingly, for the final period of excavation, when the SIMFIP mea-

468 sured mostly normal-mode opening, the potentiometer and DSS measure much larger
 469 displacements. We suggest two potential causes of this discrepancy:

- 470 1. The fault slips differently at D5 than at D7 and we cannot simply assume the SIM-
 471 FIP measurements accurately reflect movement even a few meters away. Indeed,
 472 the surface of the Main Fault is actually quite complex. For example, the upper
 473 fault interface at D5 strikes $N244^\circ$ and dips $81^\circ NW$ (possibly overturned) while
 474 in D7 it is more consistent with the overall Main Fault trend (strike $N037^\circ$, dip
 475 $64^\circ SE$; Zappone et al., 2020). The opposing dips at the two boreholes may lead
 476 to completely different slip mechanisms in response to the gallery excavation, per-
 477 haps with shear continuing at D5 where none occurs at D7.
- 478 2. The distributed nature of the potentiometer and DSS allow them to measure dif-
 479 ferent phenomena than the SIMFIP, which only senses between two points. The
 480 onset of opening mode deformation indicates a significant change in the stress state
 481 acting on the fault and may be activating fractures within the fault zone that weren't
 482 active during the shear stage, or changing their mode of deformation.

483 **7.2 Architecture and behavior of a clay-hosted fault zone**

484 The DSS measurements indicate that the two interfaces of the Main Fault zone ac-
 485 commodate most of the fault slip related to the gallery excavation, with no single, cen-
 486 tral slip surface. This is particularly evident in the inclined boreholes D3, D4, and D5
 487 (Figure 3c). In all cases, strain decays quickly away from the fault interfaces. Slip on the
 488 upper Main Fault interface, being closer to the excavation, probably relieved some of the
 489 stress that otherwise would have been transmitted to the lower interface, thereby pro-
 490 ducing an apparent gradient, with higher strain concentrated on the upper interface. In
 491 addition, this stress shadow effect may explain the lack of strain measured below the fault,
 492 even in the presence of identified fractures deeper in the boreholes. This pattern of slip
 493 on the bounding interfaces, as opposed to on a central slip surface, may relate to the Main
 494 Fault architecture.

495 Indeed, as schematized in Figure 6, fault zones are commonly conceptualized as a
 496 fault core, where the majority of the slip concentrates, and a surrounding damage zone
 497 that accommodates progressively less slip with distance from the core (Caine et al., 1996;
 498 Shipton & Cowie, 2003). The Main Fault of the MTRL, however, has an altogether dif-

499 ferent architecture, with a thick, heterogeneous layer bounded by two weak interfaces
500 (Fig. 6). These interfaces comprise a layer of fault gouge and scaly clay (up to 1 cm thick;
501 Wenning et al., 2020) that abut undisturbed Opalinus clay host rock (Jaeggi et al., 2017;
502 Nussbaum et al., 2011; Amann et al., 2018). Between the two bounding planes, the fault
503 is a complex mixture of scaly clay fabric and secondary fractures (also filled with scaly
504 clay). Outside the bounding planes is intact rock with no damage zone transition. In ad-
505 dition, previous experiments at the MTRL indicate that the fault zone has a Young’s
506 modulus 2–5 times less than the host rock (Jeanne et al., 2017). Observed DSS strains
507 may result from the high compliance of the fault zone relative to the host rock. During
508 the gallery excavation, for example, stress unloading would lead to ‘bulging’ of the fault
509 zone and slip at the interfaces. These lines of evidence suggest that the Main Fault should
510 be treated as a thick, soft layer bounded by weak boundaries and no surrounding dam-
511 age zone.

512 A number of secondary fracture sets exist within the Main Fault (Wenning et al.,
513 2020) that might produce complex deviations from deviations from the observed ‘two-
514 peaked’ pattern, for example explaining the strain measured in the fault zone at D6 (Fig-
515 ure 3C). In addition, the interaction of the bedding-parallel fracture set (cross sections;
516 Figure 5) with the Main Fault is not well understood. Given that the bedding-parallel
517 fractures represent a later stage of deformation, they may cross cut the Main Fault it-
518 self (Nussbaum et al., 2011) and accommodate some deformation affecting the Main Fault
519 interval.

520 **7.3 Stress controls on fracture activation in the Opalinus clay**

521 In many cases, the strain that accumulated on secondary (i.e. non-Main Fault) frac-
522 tures exceeded that of the Main Fault interfaces. For example, the 16-m anomaly in D3
523 displays nearly twice the displacement of the top or bottom interfaces of the Main Fault.
524 In addition, the anomalies in D4 and D5 display similar deformation magnitudes to the
525 Main Fault zone. Although a number of these secondary structures were activated, the
526 vast majority of those identified in logs were not. For a given fracture, activation is con-
527 trolled by its orientation in the local stress state and its intrinsic properties (e.g. cohe-
528 sion, coefficient of friction; Handin, 1969; Freed, 2005), but identifying which will acti-
529 vate for given stress perturbation is difficult.

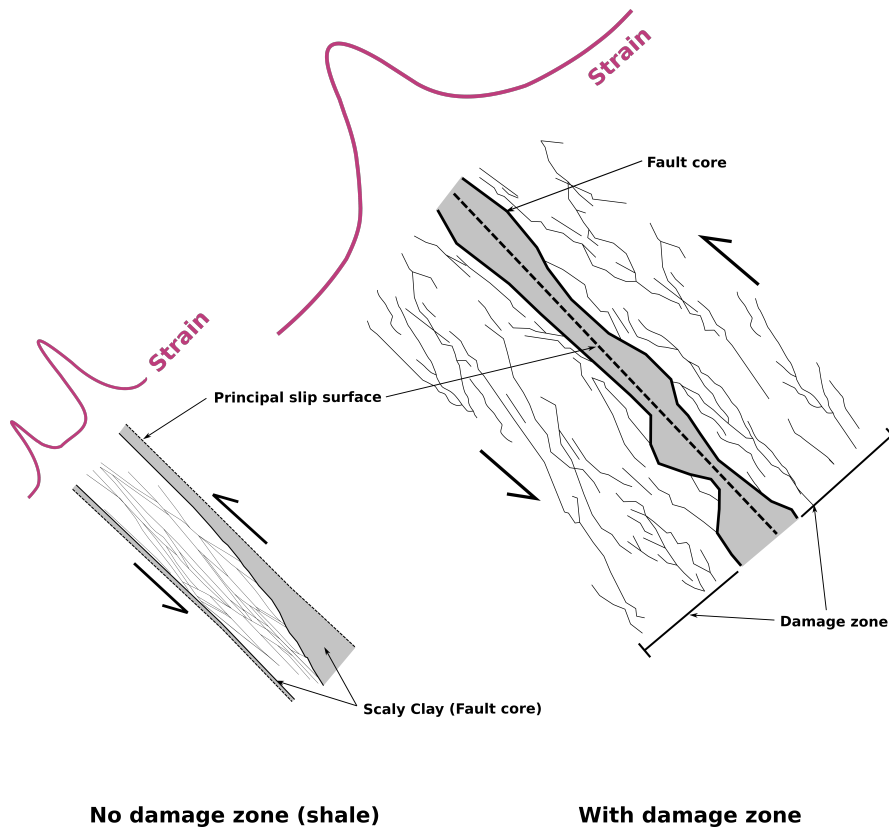


Figure 6. Schematic representations of the Main Fault (left; adapted from Jaeggi et al., 2017)) and the canonical fault zone model (right; adapted from Shipton & Cowie, 2003) showing the relationship between fault core/gouge, principal slip surfaces, and the ‘fault damage’ zone. Theoretical DSS measurements are shown in purple for slip on either type of fault.

530 Geological interpretation of the core classifies the deepest non-fault feature in BCS-
 531 D3 (16 m depth) as an interval of scaly clay layers. Optical televiewer (OTV) images
 532 for D3 were too poor for accurate picking. The single shallow feature in D4, as identi-
 533 fied in OTV logs, corresponds to a single fracture striking N052°, dipping SE69°. The
 534 15–16-m depth interval in BCS-D5 is classified as a distinct fault zone, four meters above
 535 the Main Fault (strike N014–060°, dip 20–70°SE). The 8-meter anomaly in D5 corresponds
 536 to a series of features classified as either ‘bedding’ or ‘fracture planes’ in the core (strikes
 537 N053–082°, dips 54–74°SE).

538 To investigate what distinguished the active fractures from the non-active ones, we
 539 separate all OTV-picked fractures into three groups: those inside the fault zone, active
 540 fractures outside the fault zone, and inactive fractures outside the fault zone. Figure 7
 541 shows each plane identified in the BCS-D4, D5, and D6 optical televiewer logs colored
 542 by slip tendency (increasing from blue to red) when subjected to the stress field deter-
 543 mined by Guglielmi et al. (2020) for the MTRL.

544 As detailed by Wenning et al. (2020), the Main Fault zone includes a variety of frac-
 545 ture sets of varying orientations, including fault-zone parallel fractures and WNW-dipping
 546 fractures, which are the most prone to slip of any of the identified features (red features,
 547 Figure 7A). As we mentioned above, however, slip localized on the upper and lower fault
 548 zone interfaces, which are further from failure in the in-situ stress conditions (dashed black
 549 lines and adjacent green lines, Figure 7).

550 The off-fault fractures predominantly strike NE, with dips ranging from $\sim 10\text{--}70^\circ$
 551 (Figure 7B-C). In a static stress state, the features that displayed a DSS signal are no
 552 more likely to slip than those which showed no deformation, making it difficult to dis-
 553 cern in advance, solely from OTV logs, which features would be most likely to slip. These
 554 sets of features also span the orientation of both bedding and the Main Fault zone, mean-
 555 ing we cannot confidently state whether one or the other is hosting the deformation that
 556 is being measured. This is partially an effect of the DSS spatial resolution, which pre-
 557 vents us from assigning strain to single features located within the 1-m gauge length of
 558 a DSS peak and may obscure subtle variations between slipping and non-slipping fea-
 559 tures.

560 Because the induced stress perturbation decreases with distance from the excava-
 561 tion, we color each feature in the lower row of Figure 7 by its distance from the break-

562 through point. The features in column B, associated with strain signals outside the fault
563 zone, are closer to the excavation front (on average, shown by their lighter color) than
564 either the Main Fault itself, or the features displaying no strain. This suggests that, for
565 features outside the weak fault zone, the distance to the stress perturbation has a weak
566 control on whether they activate.

567 The failure criterion used in Figure 7 assumes cohesionless fractures with a coef-
568 ficient of friction of 0.45, taken as a representative value from Opalinus core testing per-
569 formed by Orellana et al. (2018). Nearly all of the activated structures fall well below
570 the failure criterion, suggesting that either the stress perturbation from the excavation
571 was on the order of multiple MPa, that the activated fractures are actually intrinsically
572 weaker than our simple analysis suggests, or (likely) both. Careful characterization of
573 the core indicates that most of the activated structures are associated with either 1) a
574 lens of scaly clay, consisting of shear-realigned grains (Jaeggi et al., 2017; Laurich et al.,
575 2018) or 2) highly fractured zones where core was either lost or fragmented (red and blue
576 solid lines in Figure 3A, respectively). The production of scaly clay is a product of shear,
577 and produces a zone of weakness onto which further slip will tend to accumulate (Laurich
578 et al., 2018). It is therefore possible that the fractured zones also contained small amounts
579 of scaly clay that were not adequately recovered during coring and therefore were not
580 classified as such. In any case, the correlation between DSS anomalies and the depth
581 of known lenses of scaly clay (Figure 3A) suggests the presence of scaly clay is the main
582 controlling factor on fracture weakness and therefore on which features most likely to
583 activate under remote loading. At the MTRL, scaly clay has developed on both bedding
584 parallel fractures and the Main Fault-parallel structures, despite their somewhat distinct
585 orientations. This makes both sets of features susceptible to reactivation, and candidates
586 for fluid flow within the Opalinus clay.

587 **8 Conclusions**

588 We presented measurements from seven boreholes intersecting a fault zone in clay
589 rock at the Mont Terri Rock Laboratory in Switzerland. Our dataset encompasses a pe-
590 riod of new gallery excavation that remotely triggered slip within the fault and fractures
591 affecting the thick shale series. One chain potentiometer and one high-resolution 3D dis-
592 placement sensor, installed alongside the fibers, allowed us to tune the magnitudes of the
593 strain measurements made via DSS.

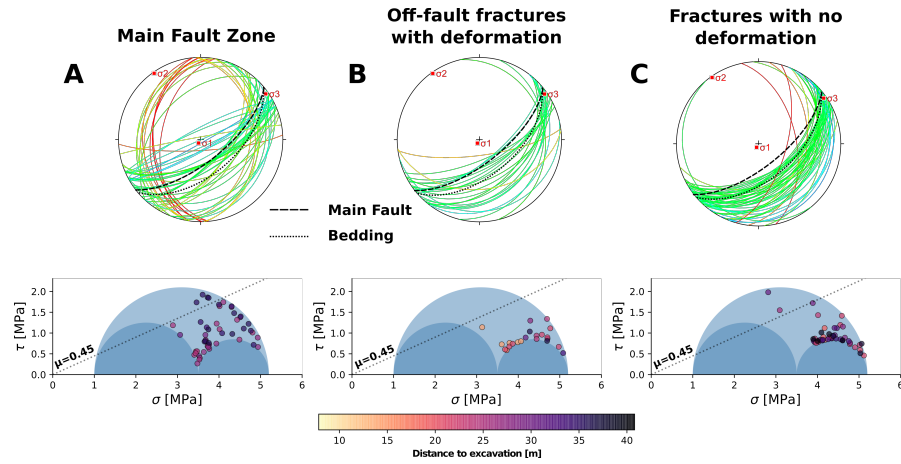


Figure 7. Fractures identified in optical televiewer logs in BCS-D4, D5, and D6 - A) Within the Main Fault zone B) outside of the Main Fault but displaying deformation on DSS C) All other fractures. The upper plots are lower hemisphere projections of poles and planes, colored by slip tendency in the local stress regime estimated by Guglielmi et al. (2020) (blue=low, red=high tendency). Dotted line shows the orientation of bedding at the MTRL, the dashed line shows the approximate orientation of the Main Fault. The lower row plots show the state of stress on each fracture relative to a Mohr Coulomb failure envelope for cohesionless fractures. Following Orellana et al. (2018), a peak coefficient of friction of $\mu=0.45$ is used. The color of each dot corresponds to the distance from the feature to the excavation front (light=closer, dark=further).

594 During the excavation, located about 30 m away from our instrumented boreholes,
595 strains ranging from 50–240 $\mu\epsilon$ were measured mainly at the top and bottom of the fault
596 zone at each of our boreholes, well above the maximum 3σ noise level of $\sim 20 \mu\epsilon$. We showed
597 that the DSS measurement has a significant sensitivity to shear strain in a grouted bore-
598 hole and thus can be used to estimate fault slip. The complex mechanical response of
599 the gallery excavation damage zone was also captured on the DSS. Indeed, our tuned mea-
600 surements also provide insight into the reactivation behavior of a clay-hosted fault.

601 The DSS measurements show that slip localized on several discrete fractures iden-
602 tified in core and logs. Within the Main Fault, slip concentrated on the upper and lower
603 fault zone interfaces, with relatively little deformation occurring inside the fault zone.
604 Core samples revealed zones of fault gouge on these interfaces, indicating past episodes
605 of slip and present-day mechanical weakness. The DSS measurements support a fault
606 model consisting of a single, thick fault zone with no surrounding damage zone. Slip oc-
607 curs at both interfaces between the fault zone and the undisturbed host rock, possibly
608 due to bulk deformation of the relatively compliant fault zone geology. This is in con-
609 trast to the canonical fault model for harder rocks where most slip occurs on a central
610 fault core surrounded by a damage zone.

611 Away from the fault, deformation concentrated at depths associated with lenses
612 of scaly clay or highly-fractured intervals (as indicated in core samples), likely on bedding-
613 parallel fractures. Most fractures identified in OTV logs were not reactivated, despite
614 nearly all having a similar orientation with respect to stress. Therefore, we conclude that
615 fracture reactivation during the excavation was controlled by the intrinsic properties of
616 the fractures, likely the presence or absence of scaly clay and fault gouge resulting in a
617 low-cohesion, low-friction surface.

618 Previous grouted DSS measurements have only proven to be of qualitative use. In
619 contrast to these previous studies, we show how a grouted network of fiber optic cables
620 can complement other monitoring systems to quantify the subsurface strain field. While
621 additional case studies like ours are necessary to expand the existing understanding of
622 these fiber optic measurements, they should prove useful in monitoring the impacts of
623 slow slip on fault-hosted leakage and induced seismicity in shales.

624 **Acknowledgments**

625 The authors are deeply grateful to the partners of the Mont Terri Project that contributed
 626 to the funding of the CS-D and FS-B experiments: the Swiss Federal Office of Topog-
 627 raphy (Swisstopo), the Swiss Federal Nuclear Safety Inspectorate (ENSI), the Japanese
 628 Atomic Energy Agency (JAEA), the Institute of Radioprotection and of Nuclear Safety
 629 (IRSN, France), TOTAL SE, CHEVRON, the Federal Institute for Geosciences and Nat-
 630 ural Resources (BGR, Hannover), the Swiss Federal Institute of Technology (ETH Zurich),
 631 and the U.S. Department of Energy. The Mont Terri Project is an international research
 632 project for the hydrogeological, geochemical, and geotechnical characterizations of a clay
 633 formation (Opalinus clay). Funding for Berkeley Lab’s analysis of the FS-B data described
 634 in this study was provided by the Assistant Secretary for Fossil Energy as part of the
 635 Core Carbon Storage and Monitoring Research (CCSMR) and National Risk Assessment
 636 Partnership (NRAP) programs of the U.S. Department of Energy under contract FP00007630.
 637 Experimental data are available in the supporting information. The CS-D experiment
 638 is part of the ACT ELEGANCY, Project No 271498. This project is supported by the
 639 Pilot and Demonstration Programme of the Swiss Federal Office of Energy (SFOE).

640 The stereonet and Mohr-Coulomb plots for Figure 7 were generated using Rick All-
 641 mendinger’s software packages Stereonet and MohrPlotter, found here: <https://www.rickallmendinger.net>
 642 (Allmendinger et al., 2011).

643 Access to the datasets presented in this paper will be made available via a pub-
 644 lic server at ETH Zurich prior to acceptance of this manuscript.

645 **References**

- 646 Allmendinger, R. W., Cardozo, N., & Fisher, D. M. (2011). *Structural Geology Al-*
 647 *gorithms*. Cambridge University Press. Retrieved from [https://doi.org/10](https://doi.org/10.1017/2Fcb09780511920202)
 648 [.1017%2Fcb09780511920202](https://doi.org/10.1017/2Fcb09780511920202) doi: 10.1017/cbo9780511920202
- 649 Amann, F., Wild, K. M., Loew, S., Yong, S., Thoeny, R., & Frank, E. (2018). Ge-
 650 omechanical behaviour of opalinus clay at multiple scales: results from mont
 651 terri rock laboratory (switzerland). In *Mont terri rock laboratory, 20 years* (pp.
 652 153–173). Springer.
- 653 Birkholzer, J. (2018). Can Induced Seismicity Cause Fault Leakage and How Does it
 654 Evolve with Time? In *14th greenhouse gas control technologies conference mel-*

655 *bourne* (pp. 21–26).

656 Bossart, P., Bernier, F., Birkholzer, J., Bruggeman, C., Connolly, P., Dewonck, S.,
 657 ... Wiczorek, K. (2017, dec). Mont Terri rock laboratory 20 years of re-
 658 search: introduction, site characteristics and overview of experiments. In *Mont*
 659 *terri rock laboratory, 20 years* (pp. 3–22). Springer International Publishing.
 660 Retrieved from https://doi.org/10.1007/978-3-319-70458-6_1 doi:
 661 10.1007/978-3-319-70458-6_1

662 Bourg, I. C. (2015). Sealing shales versus brittle shales: a sharp threshold in the
 663 material properties and energy technology uses of fine-grained sedimentary
 664 rocks. *Environmental Science & Technology Letters*, *2*(10), 255–259.

665 Caine, J. S., Evans, J. P., & Forster, C. B. (1996). Fault zone architecture and per-
 666 meability structure. *Geology*, *24*(11), 1025–1028.

667 Corkum, A., & Martin, C. (2007, sep). Modelling a mine-by test at the Mont
 668 Terri rock laboratory Switzerland. *International Journal of Rock Mechanics*
 669 *and Mining Sciences*, *44*(6), 846–859. Retrieved from [https://doi.org/](https://doi.org/10.1016/j.ijrmms.2006.12.003)
 670 [10.1016/j.ijrmms.2006.12.003](https://doi.org/10.1016/j.ijrmms.2006.12.003) doi: 10.1016/j.ijrmms.2006.12.003

671 Delepine-Lesoille, S., Phéron, X., Bertrand, J., Pilorget, G., Hermand, G., Farhoud,
 672 R., ... Lanticq, V. (2012). Industrial Qualification Process for Optical Fibers
 673 Distributed Strain and Temperature Sensing in Nuclear Waste Reposito-
 674 ries. *Journal of Sensors*, *2012*, 1–9. Retrieved from [https://doi.org/](https://doi.org/10.1155/2012/369375)
 675 [10.1155/2012/369375](https://doi.org/10.1155/2012/369375) doi: 10.1155/2012/369375

676 Freed, A. M. (2005, may). EARTHQUAKE TRIGGERING BY STATIC
 677 DYNAMIC AND POSTSEISMIC STRESS TRANSFER. *Annual Re-*
 678 *view of Earth and Planetary Sciences*, *33*(1), 335–367. Retrieved from
 679 <https://doi.org/10.1146/annurev.earth.33.092203.122505> doi:
 680 10.1146/annurev.earth.33.092203.122505

681 Guglielmi, Y., Birkholzer, J., Rutqvist, J., Jeanne, P., & Nussbaum, C. (2017, jul).
 682 Can Fault Leakage Occur Before or Without Reactivation? Results from an
 683 in Situ Fault Reactivation Experiment at Mont Terri. *Energy Procedia*, *114*,
 684 3167–3174. Retrieved from [https://doi.org/10.1016/j.egypro.2017.03](https://doi.org/10.1016/j.egypro.2017.03.1445)
 685 [.1445](https://doi.org/10.1016/j.egypro.2017.03.1445) doi: 10.1016/j.egypro.2017.03.1445

686 Guglielmi, Y., Cappa, F., Lançon, H., Janowczyk, J. B., Rutqvist, J., Tsang,
 687 C. F., & Wang, J. S. Y. (2013). ISRM Suggested Method for Step-Rate

- 688 Injection Method for Fracture In-Situ Properties (SIMFIP): Using a 3-
689 Components Borehole Deformation Sensor. In *The ISRM suggested meth-*
690 *ods for rock characterization testing and monitoring: 2007-2014* (pp. 179–
691 186). Springer International Publishing. Retrieved from [https://doi.org/](https://doi.org/10.1007/978-3-319-07713-0_14)
692 [10.1007/978-3-319-07713-0_14](https://doi.org/10.1007/978-3-319-07713-0_14) doi: 10.1007/978-3-319-07713-0_14
- 693 Guglielmi, Y., Nussbaum, C., Jeanne, P., Rutqvist, J., Cappa, F., & Birkholzer,
694 J. (2020, feb). Complexity of Fault Rupture and Fluid Leakage in Shale:
695 Insights From a Controlled Fault Activation Experiment. *Journal of Geo-*
696 *physical Research: Solid Earth*, 125(2). Retrieved from [https://doi.org/](https://doi.org/10.1029/2019jb017781)
697 [10.1029/2019jb017781](https://doi.org/10.1029/2019jb017781) doi: 10.1029/2019jb017781
- 698 Guglielmi, Y., Nussbaum, C., Robertson, M., Ajo-Franklin, J., Zappone, A., Klop-
699 penburg, A., & Birkholzer, J. (2018). *FS-B Experiment: Imaging the long-term*
700 *loss of faulted host rock integrity - Test plan, Mont Terri Technical Note* (Tech.
701 Rep. No. TN2018-20).
- 702 Gutierrez, M., Øino, L., & Nygaard, R. (2000). Stress-dependent permeability of
703 a de-mineralised fracture in shale. *Marine and Petroleum Geology*, 17(8), 895–
704 907.
- 705 Handin, J. (1969, oct). On the Coulomb-Mohr failure criterion. *Journal of Geophys-*
706 *ical Research*, 74(22), 5343–5348. Retrieved from [https://doi.org/10.1029/](https://doi.org/10.1029/2019jb017781)
707 [2019jb017781](https://doi.org/10.1029/2019jb017781) doi: 10.1029/jb074i022p05343
- 708 Hartog, A. H. (2017). *An Introduction to Distributed Optical Fibre Sensors*. CRC
709 Press. Retrieved from <https://doi.org/10.1201/9781315119014> doi: 10
710 .1201/9781315119014
- 711 Horiguchi, T., & Tateda, M. (1989). BOTDA-nondestructive measurement of
712 single-mode optical fiber attenuation characteristics using Brillouin interaction:
713 theory. *Journal of Lightwave Technology*, 7(8), 1170–1176. Retrieved from
714 <https://doi.org/10.1109/50.32378> doi: 10.1109/50.32378
- 715 Hostettler, B., Reisdorf, A. G., Jaeggi, D., Deplazes, G., Bläsi, H., Morard, A.,
716 ... Menkveld-Gfeller, U. (2017, feb). Litho- and biostratigraphy of the
717 Opalinus Clay and bounding formations in the Mont Terri rock labora-
718 tory (Switzerland). *Swiss Journal of Geosciences*, 110(1), 23–37. Re-
719 trieved from <https://doi.org/10.1007/s00015-016-0250-3> doi:
720 10.1007/s00015-016-0250-3

- 721 Iten, M., Puzrin, A. M., & Schmid, A. (2008, mar). Landslide monitoring using a
 722 road-embedded optical fiber sensor. In W. Ecke, K. J. Peters, & N. G. Meyen-
 723 dorf (Eds.), *Smart sensor phenomena technology, networks, and systems*
 724 *2008*. SPIE. Retrieved from <https://doi.org/10.1117/12.774515> doi:
 725 10.1117/12.774515
- 726 Jaeggi, D., Laurich, B., Nussbaum, C., Schuster, K., & Connolly, P. (2017, jan).
 727 Tectonic structure of the “Main Fault” in the Opalinus Clay Mont Terri
 728 rock laboratory (Switzerland). *Swiss Journal of Geosciences*, *110*(1), 67–
 729 84. Retrieved from <https://doi.org/10.1007/s00015-016-0243-2> doi:
 730 10.1007/s00015-016-0243-2
- 731 Jeanne, P., Guglielmi, Y., Rutqvist, J., Nussbaum, C., & Birkholzer, J. (2017). Field
 732 characterization of elastic properties across a fault zone reactivated by fluid
 733 injection. *Journal of Geophysical Research: Solid Earth*, *122*(8), 6583–6598.
- 734 jun Wang, B., Li, K., Shi, B., & qing Wei, G. (2008, sep). Test on application of
 735 distributed fiber optic sensing technique into soil slope monitoring. *Landslides*,
 736 *6*(1), 61–68. Retrieved from [https://doi.org/10.1007/s10346-008-0139-](https://doi.org/10.1007/s10346-008-0139-y)
 737 [y](https://doi.org/10.1007/s10346-008-0139-y) doi: 10.1007/s10346-008-0139-y
- 738 Krietsch, H., Gischig, V., Jalali, M., Doetsch, J., Valley, B., Amann, F., et al.
 739 (2018). A comparison of FBG-and Brillouin-strain sensing in the frame-
 740 work of a decameter-scale hydraulic stimulation experiment. In *52nd us rock*
 741 *mechanics/geomechanics symposium*.
- 742 Laurich, B., Urai, J. L., Vollmer, C., & Nussbaum, C. (2018). Deformation mecha-
 743 nisms and evolution of the microstructure of gouge in the main fault in opali-
 744 nus clay in the mont terri rock laboratory (ch). *Solid Earth*, *9*(1), 1–24.
- 745 Madjdabadi, B., Valley, B., Dusseault, M., & Kaiser, P. (2014). Numerical study
 746 of grout–rock mass interaction effect on distributed optical fibre sensor mea-
 747 surements. In *Proceedings of the seventh international conference on deep and*
 748 *high stress mining*. Australian Centre for Geomechanics Perth. Retrieved
 749 from https://doi.org/10.36487/acg_rep%2F1410_31_madjdabadi doi:
 750 10.36487/acg_rep/1410_31_madjdabadi
- 751 Madjdabadi, B., Valley, B., Dusseault, M. B., & Kaiser, P. K. (2016, jan). Ex-
 752 perimental evaluation of a distributed Brillouin sensing system for measuring
 753 extensional and shear deformation in rock. *Measurement*, *77*, 54–66. Re-

- 754 retrieved from <https://doi.org/10.1016/j.measurement.2015.08.040> doi:
755 10.1016/j.measurement.2015.08.040
- 756 Naruse, H. (1999, sep). River levee strain measurement using fiber optic dis-
757 tributed strain sensor. In *13th international conference on optical fiber sen-*
758 *sors*. SPIE. Retrieved from <https://doi.org/10.1117/12.2302056> doi:
759 10.1117/12.2302056
- 760 Naruse, H., Komatsu, K., Fujihashi, K., & Okutsu, M. (2005, may). Telecom-
761 munications tunnel monitoring system based on distributed optical fiber
762 strain measurement. In *17th international conference on optical fibre sen-*
763 *sors*. SPIE. Retrieved from <https://doi.org/10.1117/12.623645> doi:
764 10.1117/12.623645
- 765 Nussbaum, C., Bossart, P., Amann, F., & Aubourg, C. (2011, sep). Analy-
766 sis of tectonic structures and excavation induced fractures in the Opalinus
767 Clay Mont Terri underground rock laboratory (Switzerland). *Swiss Jour-*
768 *nal of Geosciences*, *104*(2), 187–210. Retrieved from [https://doi.org/](https://doi.org/10.1007/s00015-011-0070-4)
769 10.1007/s00015-011-0070-4 doi: 10.1007/s00015-011-0070-4
- 770 Orellana, L., Scuderi, M., Collettini, C., & Violay, M. (2018). Frictional properties
771 of opalinus clay: Implications for nuclear waste storage. *Journal of Geophysical*
772 *Research: Solid Earth*, *123*(1), 157–175.
- 773 Rinaldi, A. P., Guglielmi, Y., Zappone, A., Soom, F., Robertson, M., Cook, P., ...
774 Nussbaum, C. (2020, mar). Coupled processes in clay during tunnel exca-
775 vation. Copernicus GmbH. Retrieved from [https://doi.org/10.5194/](https://doi.org/10.5194/egusphere-egu2020-18041)
776 2Fegusphere-egu2020-18041 doi: 10.5194/egusphere-egu2020-18041
- 777 Shipton, Z. K., & Cowie, P. A. (2003). A conceptual model for the origin of fault
778 damage zone structures in high-porosity sandstone. *Journal of Structural Geol-*
779 *ogy*, *25*(3), 333–344.
- 780 Sun, Y., Xue, Z., Hashimoto, T., Lei, X., & Zhang, Y. (2020, jan). Distributed
781 Fiber Optic Sensing System for Well-Based Monitoring Water Injection
782 Tests—A Geomechanical Responses Perspective. *Water Resources Research*,
783 *56*(1). Retrieved from <https://doi.org/10.1029/2019wr024794> doi:
784 10.1029/2019wr024794
- 785 Tateda, M., Horiguchi, T., Kurashima, T., & Ishihara, K. (1990). First mea-
786 surement of strain distribution along field-installed optical fibers using Brill-

- 787 loun spectroscopy. In *Optical fiber communication*. OSA. Retrieved from
788 <https://doi.org/10.1364%2Fofc.1990.pd15> doi: 10.1364/ofc.1990.pd15
- 789 Valley, B., Madjdabadi, B. M., Kaiser, P. K., Dusseault, M. B., et al. (2012). Moni-
790 toring mining-induced rock mass deformation using distributed strain monitor-
791 ing based on fiber optics. In *Ism international symposium-eurock 2012*.
- 792 Wenning, Q. C., Madonna, C., Zappone, A., Grab, M., Rinaldi, A. P., Plötze, M.,
793 ... Wiemer, S. (2020). Shale fault zone structure and stress dependent
794 anisotropic permeability and seismic velocity properties (opalinus clay, switzer-
795 land). *Journal of Structural Geology*, 104273.
- 796 Zappone, A., Rinaldi, A. P., Grab, M., Wenning, Q., Roques, C., Madonna, C., ...
797 others (2020). Fault sealing and caprock integrity for co 2 storage: an in-situ
798 injection experiment. *Solid Earth Discussions*, 1–51.
- 799 Zhang, C.-C., Shi, B., Gu, K., Liu, S.-P., Wu, J.-H., Zhang, S., ... Wei, G.-Q. (2018,
800 nov). Vertically Distributed Sensing of Deformation Using Fiber Optic Sensing.
801 *Geophysical Research Letters*, 45(21), 11,732–11,741. Retrieved from [https://](https://doi.org/10.1029%2F2018gl080428)
802 doi.org/10.1029%2F2018gl080428 doi: 10.1029/2018gl080428
- 803 Zhang, Z., Fang, Z., Stefani, J., DiSiena, J., Bevc, D., Ning, I. L. C., ... Tan,
804 Y. (2020, aug). Modeling of Fiber Optic Strain Responses to Hydraulic
805 Fracturing. *GEOPHYSICS*, 1–22. Retrieved from [https://doi.org/](https://doi.org/10.1190%2Fgeo2020-0083.1)
806 [10.1190%2Fgeo2020-0083.1](https://doi.org/10.1190%2Fgeo2020-0083.1) doi: 10.1190/geo2020-0083.1
- 807 Zhou, Z., He, J., Huang, M., He, J., Ou, J., & Chen, G. (2010, mar). Cas-
808 ing pipe damage detection with optical fiber sensors: a case study in oil
809 well constructions. In P. J. Shull, A. A. Diaz, & H. F. Wu (Eds.), *Non-*
810 *destructive characterization for composite materials aerospace engineering,*
811 *civil infrastructure, and homeland security 2010*. SPIE. Retrieved from
812 <https://doi.org/10.1117%2F12.848727> doi: 10.1117/12.848727
- 813 Zoback, M. D., Kohli, A., Das, I., McClure, M. W., et al. (2012). The importance
814 of slow slip on faults during hydraulic fracturing stimulation of shale gas reser-
815 voirs. In *Spe americas unconventional resources conference*.